American Journal of Analytical Chemistry, 2017, 8, 60-71
http://www.scirp.org/journal/ajac
ISSN Online: 2156-8278
ISSN Print: 2156-8251

# Influence of Mn Doping on the Sensing Properties of $SnO_2$ Nanobelt to Ethanol

**Jieqing Huang[1,2], Yingkai Liu[1,2,3*], Yuemei Wu[1,2], Xinmin Li[1,2]**

[1]Key Laboratory of Yunnan Higher Education Institutes for Optoelectric Information & Technology, Kunming, China
[2]Institute of Physics and Electronic Information, Yunnan Normal University, Kunming, China
[3]Key Laboratory of Yunnan Normal University for Photoelectric Materials & Device, Kunming, China
Email: huangjieqing608@163.com, *ykliu@ynnu.edu.cn, wuyuemei893@163.com, lixinmin809@163.com

**How to cite this paper:** Huang, J.Q., Liu, Y.K., Wu, Y.M. and Li, X.M. (2017) Influence of Mn Doping on the Sensing Properties of $SnO_2$ Nanobelt to Ethanol. *American Journal of Analytical Chemistry*, **8**, 60-71.
http://dx.doi.org/10.4236/ajac.2017.81005

**Received:** December 7, 2016
**Accepted:** January 9, 2017
**Published:** January 12, 2017





## Abstract

Mn doped $SnO_2$ nanobelts (Mn:$SnO_2$ NBs) and pure $SnO_2$ nanobelts ($SnO_2$ NBs) were synthesized by thermal evaporation technique at 1355˚C with Ar carrier gas (25 sccm, 150 Torr). The SEM, EDS, XRD, TEM, HRTEM, SAED, XPS, UV-Vis techniques were used to characterize the attained samples. The band gap of Mn doped $SnO_2$ NBs by UV-Vis was measured to be 3.43 eV at room temperature, lower than that of the pure counterpart with ~3.66 eV. Mn:$SnO_2$ NB and pure $SnO_2$ NB sensors were developed. It is found that Mn:$SnO_2$ NB device exhibits a higher sensitivity with 62.12% to 100 ppm of ethanol at 210˚C, which is the highest sensitivity among the three tested VOC gases (ethanol, ethanediol, and acetone). The theoretical detection limit for ethanol of the sensor is 1.1 ppm. The higher response is related to the selective catalysis of the doped Mn ions.

## Keywords

$SnO_2$ Nanobelts, $Mn^{3+}$ Doping, Gas Sensor, Single Nanobelt Device

## 1. Introduction

Metal-oxide semiconductor gas sensors have been used to detect gases for their efficiency and spread applicability [1] [2]. In particular, one-dimensional semiconductor nanostructures, such as nanobelt, nanowire and nanotube, due to their unique physical and chemical properties caused by their nanometer size effect, have aroused great interest due to their unique characteristics [3] [4] [5] [6] [7]. Therefore, metal-oxide semiconductor nanostructured materials, such as $SnO_2$, $In_2O_3$, $WO_3$ and ZnO, have been widely manufactured as sensors for de-

tecting air composition and organic or poisonous gases due to low cost, easy accessibility, high performance, and reliable stability [8] [9] [10] [11]. Among them, $SnO_2$ with a band gap (3.6 eV), has high sensitivity and fast response [12]. Hence, $SnO_2$ nanomaterials have been investigated to detect many gases, such as ethanol, $H_2S$, and so on [13] [14] [15]. It is well known that the dopant of rare metals may improve the sensitive performance of nanomaterials [16]. For instance, Li *et al.* have reported that the sensitivity of Er-doped $SnO_2$ nanobelt device is 9 to the formaldehyde gas [17]. Ma *et al.* have found that the response of Sb-doped $SnO_2$ nanoribbon device reaches 56 (10) to 100 ppm (ppb) of $H_2S$ at 150˚C and 19 (1.6) to 100 ppm (ppb) of $H_2S$ at 25˚C [18].

Doping enhances the properties of semiconductors by providing a powerful strategy to control their optical, electronic, transport, and spintronic properties [19]. The optoelectronic properties such as photoluminescence and optical band gap of $SnO_2$ can also be improved by metals doping. Many studies were reported on the $SnO_2$ doped by Sb, In, and Mn etc. [20] [21] [22]. Much emphasis is put on manganese (Mn) due to its large equilibrium solubility and nearly the same ionic radii as with $Sn^{4+}$ ion for substitution.

In this paper, we systemically investigated the sensing and optical properties of a single Mn:$SnO_2$ NB sensor to volatile organic (VOC) liquids and reported interesting results.

## 2. Experimental Section

### 2.1. Synthesis and Characterization of $SnO_2$ NBs and Mn:$SnO_2$ NBs

Single $SnO_2$ and Mn:$SnO_2$ NBs were obtained by thermal evaporation method. For the synthesis of Mn:$SnO_2$ NBs, the mixture of pure $SnO_2$ powders (>99.99 wt.%) and $MnC_2O_4{\cdot}2H_2O$ powders premixed in the weight ratio of 20:1 was put into a ceramic boat. The ceramic boat was placed into the central position of the horizontal alundum tube, which was put into a high temperature furnace. A silicon substrate coated with about 10 nm Au film was placed into the tube, the distance of silicon substrate and ceramic boat was about 15 cm. After cleaning the tube several times with nitrogen gas, the tube was evacuated by a mechanical pump to a pressure of 1 to 5 Pa. The precursors of $SnO_2$ and $MnC_2O_4{\cdot}2H_2O$ powders were maintained at 1355˚C for 2 h and deposited on the Si substrate with Ar carrier gas (25 sccm, the pressure inside the tube is 150 Torr). After the furnace was cooled to room temperature naturally, white wool-like products were obtained. In order to compare the sensing properties of Mn:$SnO_2$ NBs and pure $SnO_2$ NBs, we also prepared pure $SnO_2$ NBs by similar method.

The nanobelts were characterized by scanning electron microscopy (SEM) and energy-dispersive X-ray spectroscopy (EDS), X-ray diffraction (XRD), transmission electron microscopy (TEM) and high-resolution electron microscopy (HRTEM), selected area electron diffraction (SAED), X-ray photoelectron spectrometer (XPS), and ultraviolet and visible spectrophotometer (UV-Vis).

### 2.2. The Manufacture and Characterization of a Single Nanobelt Gas Sensor

$SnO_2$ NBs and Mn:$SnO_2$ NBs were picked out and then dispersed into ethanol by the tweezers. A few of the resulting suspensions were dropped onto a silicon substrate with thickness of a 500 nm $SiO_2$ layer. The suspensions dried naturally and led to the nanobelts stick to the substrate closely. The mask plate was placed on the top of this substrate to prepare the electrodes. Patterned Ti (10 nm) and Au (100 nm) electrodes were successively deposited on the nanobelts in high vacuum by dual-ion beam sputtering (LDJ-2a-F100-100 series) with Ar carrier gas (10 mA/cm$^2$, $2.2 \times 10^{-2}$ Pa).

The measurement of the gas sensor was processed with the equipment designed by our laboratory [23]. The process was conducted in a hermetic stainless steel box (20 L). Then, the device was put on a heating station, on which its temperature can be accurately controlled. The sensing properties of the device were measured by Keithley 4200 semiconductor test system. The applied bias voltage was 1 V and the testing interval was 200 seconds. The target liquid can be injected into a heater to evaporate the VOC liquid violently and the fan was used to produce a homogeneous atmosphere in the chamber. The optical microscopic image of a single nanobelt device is displayed in Figure 1.

## 3. Results and Discussion

### 3.1. Structural Characterization

#### 3.1.1. SEM and HRTEM

The morphology of the as-synthesized materials is displayed in Figure 2. Mn:$SnO_2$ NBs and $SnO_2$ NBs have similar morphology. Figure 2(a), Figure 2(b) are SEM micrographs of Mn:$SnO_2$ NBs by low and high magnifications. The product consists of a large quantity of ribbon-like structures with different thickness and width, as shown in Figure 2(a). Most of the nanobelts have uniform thickness and width. Figure 2(b) depicts that their thickness is less than

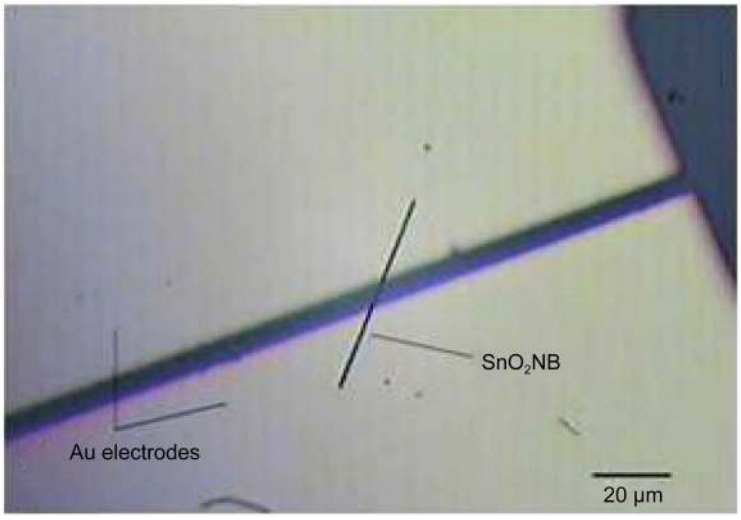


Figure 1. The microscope photograph of a prepared $SnO_2$ NB device.

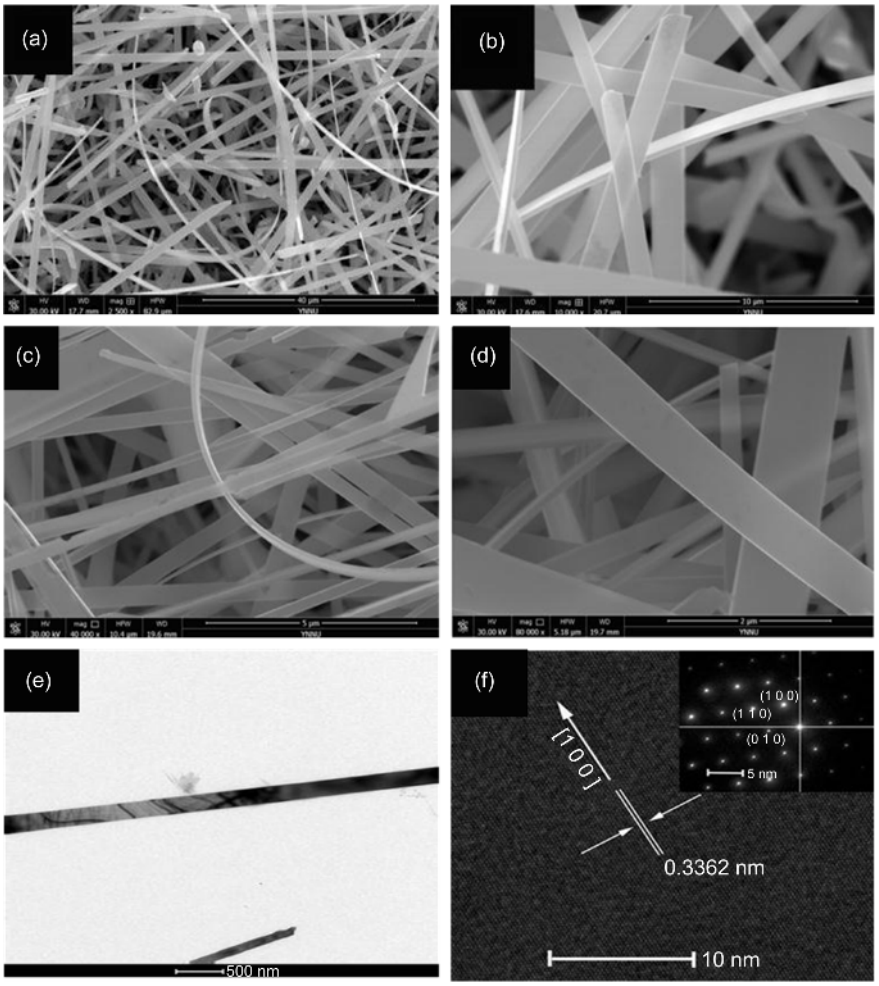


**Figure 2.** (a) Low and (b) high magnification SEM micrograph of Mn:$SnO_2$ NBs. (c) Low and (d) high magnification SEM micrograph of $SnO_2$ NBs. (e) TEM image of Mn:$SnO_2$ NB. (f) HRTEM image of Mn:$SnO_2$ NB, its inset is SAED pattern.

100 nm, the width is from 250 nm to 1 μm, and the length is about 50 μm. It is also seen that the Mn:$SnO_2$ NBs have a good shape with smooth surface, which are suitable for preparing gas sensors. Figure 2(c) is SEM image of $SnO_2$ NBs by low magnification, it can be obviously seen that the $SnO_2$ NBs are band-like structure, the length of them is about 30 - 100 μm. Figure 2(d) is a high magnification SEM micrograph of $SnO_2$ NBs, the $SnO_2$ NBs have smooth surface, the width is less than 1 μm, and thickness is about 50 - 100 nm.

For further characterizing their microstructure, we carried out TEM, HRTEM and SAED examination and are presented in Figure 2(e) and Figure 2(f). TEM image illustrates that the width of a selected NB is about 300 nm. Figure 2(d) presents HRTEM image of a single Mn:$SnO_2$ NB and its corresponding SAED pattern. It is seen that the interplanar spacing is 0.3362 nm, matching with the (1 0 0) plane for tetragonal structure $SnO_2$, no defects have been detected. The regular arrangement of the diffraction spots is shown in the upper-right inset of Figure 2(d), revealing that the growth direction of Mn:$SnO_2$ NBs is along [1 0 0].

### 3.1.2. XRD and EDS

XRD pattern of Mn:$SnO_2$ NBs is presented in **Figure 3(a)**. The diffraction peaks can be indexed as the tetragonal structure $SnO_2$ with lattice parameters a = b = 0.4738 nm, c = 0.3189 nm (JCPDS file No. 71-0467).

In order to decide whether Mn ions were doped into $SnO_2$ NBs or not, energy-dispersive X-ray diffraction spectroscopy (EDS) pattern of a single Mn:$SnO_2$ NB is conducted, as shown in **Figure 3(b)**. It is seen that the doped Mn ions content of $SnO_2$ NBs is only 1.64 at.%. The Sn and O atomic percentage is 1:1.8, which is smaller than tin dioxide stoichiometric ratio (1:2), indicating that there are oxygen vacancies in the sample.

### 3.1.3. XPS Analysis

The XPS observation of as-prepared Mn:$SnO_2$ sample is shown in **Figure 4(a)**. From the global XPS profiles, the lines related to Sn, O, Mn, and C elements are observed. Carbon is ubiquitously presented on all surfaces for XPS spectra. It is well known that the peak at 285.0 eV of carbon C 1 s is used as a reference for charge correction. The Sn(3d) band presents double peaks located at binding energies of 487.0 of Sn($3d_{5/2}$) and 495.4 eV of Sn($3d_{3/2}$), as shown in **Figure 4(b)**. The separation distance between the two peaks is 8.4 eV, which confirms the formation of $Sn^{4+}$ oxidation state in $SnO_2$ nanobelts [24]. The Mn (2p) state can be separated into two peaks. One is centered at 640.0 eV, the other at 644.9 eV, as displayed in **Figure 4(c)**.

The deconvolution of the O (1s) peak shows two Gaussian peaks centered at 530.9 and 531.7eV, respectively (as illustrated in **Figure 4(d)**). The peak located at the lower binding energy corresponds to the O (1 s) core peak of $O^{2-}$ bound to $Sn^{4+}$ and the other one at higher binding energy originates from O defects [25].

$$\frac{n_{Sn}}{n_O} = \frac{I_{Sn}}{I_O} \times \frac{S_O}{S_{Sn}}$$

$S_{Sn}$ and $S_O$ are sensitive factors ($S_{Sn}$ = 4.095, $S_0$ = 0.711); $I_{Sn}$ and $I_O$ are the peak areas; $n_{Sn}$ and $n_O$ are atomic concentrations on behalf of *Sn* and *O* elements, respectively. The ratio of $n_{Sn}$ and $n_O$ is 0.56 by fitting. However, the ratio of $n_{Sn}$ and $n_O$ in pure $SnO_2$ is 0.5. It is further corroborated that the Mn:$SnO_2$ NBs have oxygen vacancies.

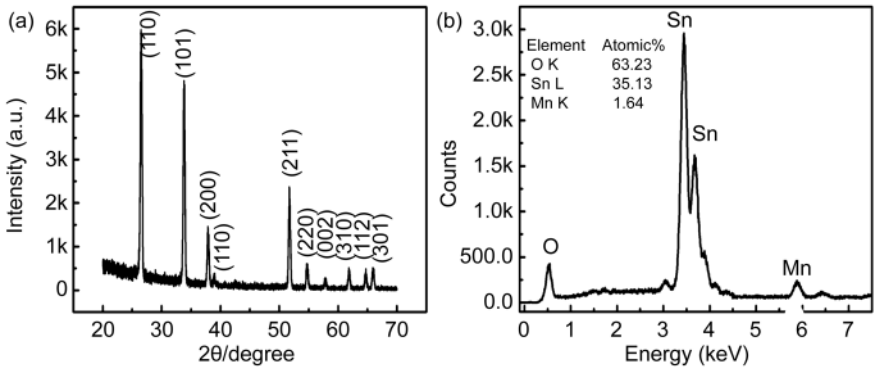


**Figure 3.** (a) XRD of Mn:$SnO_2$ NBs. (b) EDS of Mn:$SnO_2$ NB.

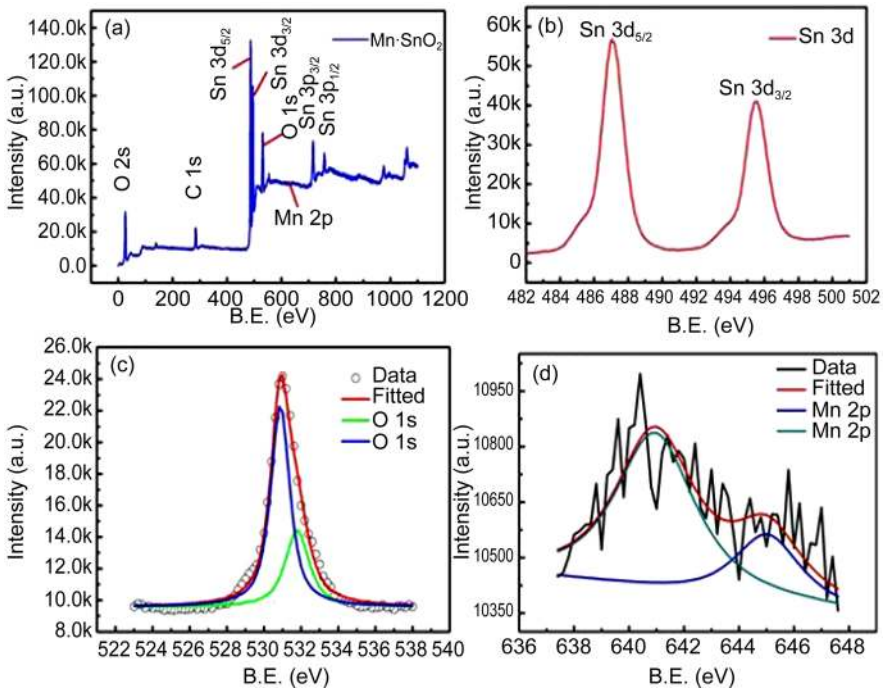


**Figure 4.** XPS spectra of the Mn:$SnO_2$. (a) global survey spectra and high-solution (b) Sn 3d, (c) O 1 s and (d) Mn 2p spectrum.

### 3.2. UV-Vis Spectra

The optical absorption coefficient $\alpha$ of a semiconductor close to the band edge can be expressed by the following Wood-Tauc Equation [26]:

$$\alpha = k\left(h\nu - E_g\right)^n / h\nu$$

where $\alpha$ is the absorption coefficient, $k$ is a constant about material properties, $h\nu$ is the energy of a photon, $E_g$ is band gap, and $n$ is a parameter that depends on the nature of the transition. In this case, $n$ is equal to 1/2 for a direct bandgap material. The band gap can be estimated from a plot of $(\alpha h\nu)^2$ versus photon energy.

**Figure 5** shows the absorption spectra of Mn:$SnO_2$ NBs and $SnO_2$ NBs. The band gaps (Eg) of Mn:$SnO_2$ NBs and $SnO_2$ NBs are 3.43 and 3.66 eV, respectively. The shift may be due to the quantum size effect. The plots of $(\alpha h\nu)^2$ as a function of the energy ($h\nu$) of the incident radiation for Mn:$SnO_2$ NBs and $SnO_2$ NBs are presented in the inset of **Figure 5**. All plots show non-linear nature. Compared with that of $SnO_2$ NBs, the redshift is observed in the absorption edge of Mn:$SnO_2$ NBs. The change on the bandgap suggests that the size of the nanobelt has an influence on the optical properties of the materials, which can be tuned by doping.

### 3.3. Sensing Properties

The sensor's response is defined as the relative change of resistance in the surrounding gas atmosphere divided by the resistance in synthetic air [27], which is defined as

$$S\% = \frac{Ra - Rg}{Ra} \times 100\% = \left(1 - \frac{Rg}{Ra}\right) \times 100\%$$

In the formula of $S(\%)$, $R_a$ is the sensor resistance in the air and $R_g$ is the resistance in the tested gas.

The curves exhibit a linear shape, so both doped and pure NBs possess a good Ohmic contact, as shown in Figure 6. The slope of pure $SnO_2$ NB is less than that of Mn:$SnO_2$ NB. The resistances of Mn:$SnO_2$ NB and its pure counterpart are about $1.65 \times 10^8$ Ω and $1.61 \times 10^9$ Ω respectively at 210˚C, indicating that the resistance of $SnO_2$ is greatly reduced after doping.

Upon exposed to 100 ppm of ethanol, ethanediol, and acetone gases, the responses of the sensors based on Mn:$SnO_2$ NB and its undoped counterpart have been tested as a function of the temperatures from 50˚C to 300˚C, as shown in Figure 7(a), Figure 7(b). The best operating temperature of Mn:$SnO_2$ NB to the three gases is 210˚C and the responses to ethanol, ethanediol, and acetone are

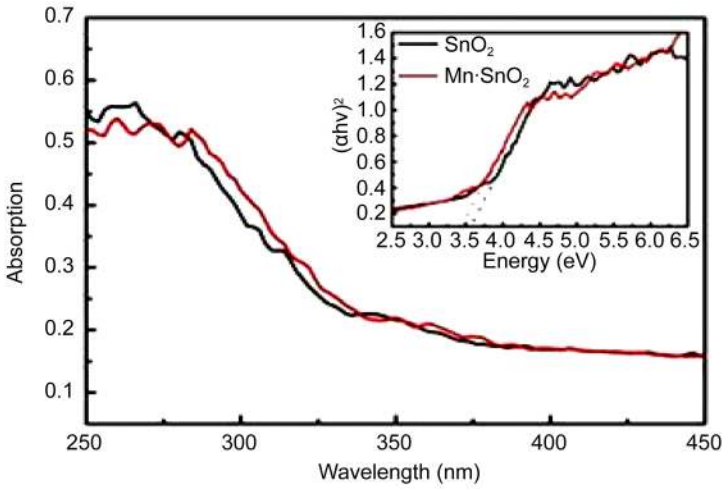


Figure 5. The UV absorption spectra of Mn:$SnO_2$ NBs and $SnO_2$ NBs.

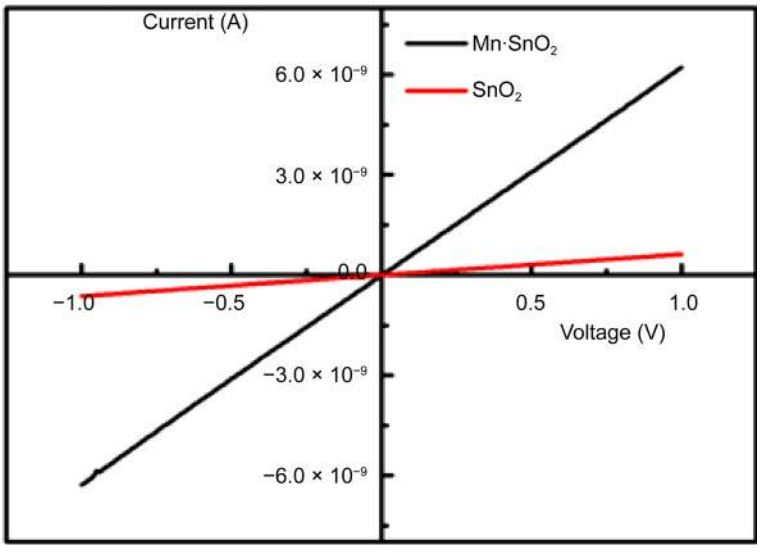


Figure 6. I-V curves of pure $SnO_2$ NB and Mn:$SnO_2$ NB devices.

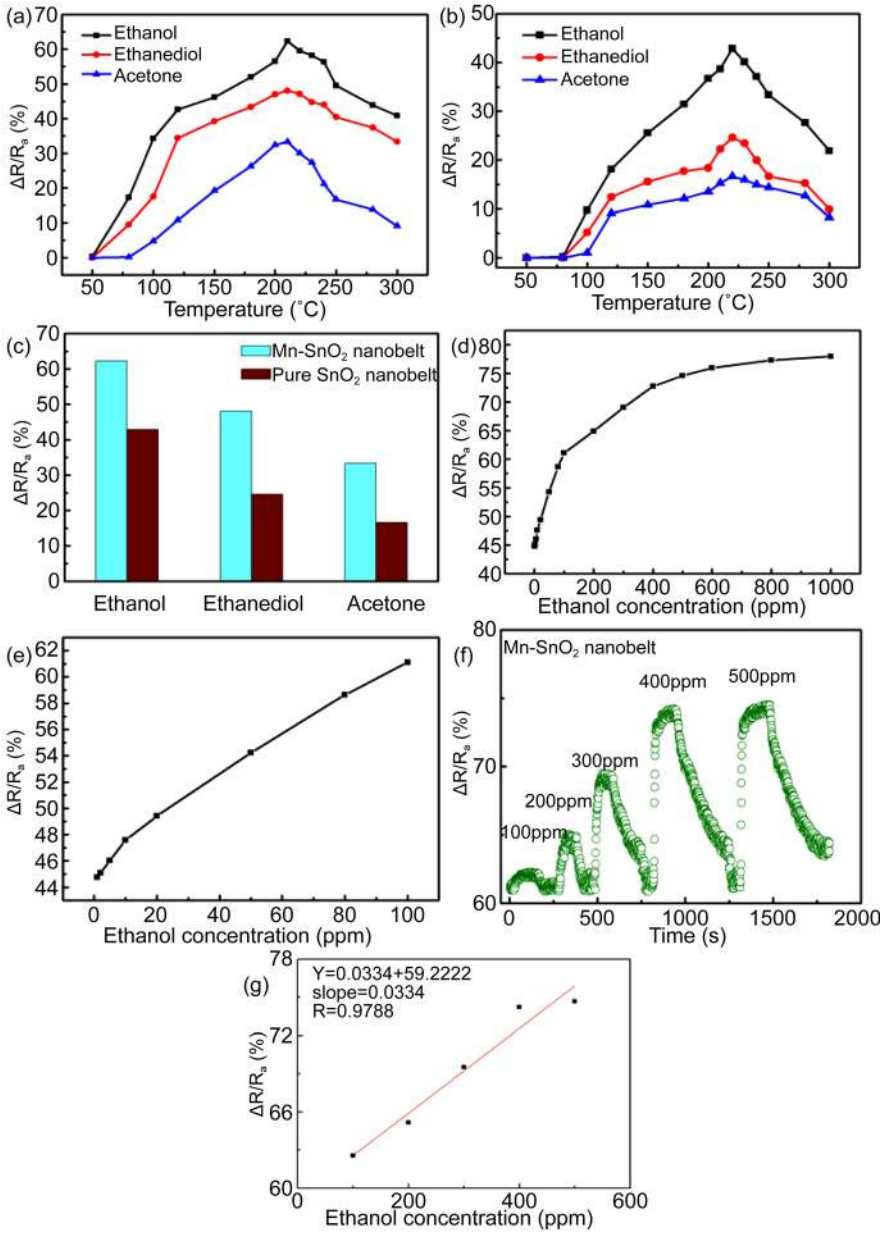


Figure 7. (a) and (b) The gas sensitivity of Mn:$SnO_2$ NB and pure $SnO_2$ NB to 100 ppm of various gases at different temperature; (c) Histogram sensitive responses of Mn:$SnO_2$ NB and pure $SnO_2$ NB at 210˚C; (d) The sensitivity of Mn:$SnO_2$ NB to ethanol from 5 to 1000 ppm at 210˚C; (e) The curve of response versus ethanol concentration in the range of 5 - 100 ppm; (f) Responses to 100 - 500 ppm of ethanol at 210˚C; (g) The fitting curve of response versus ethanol concentration in the range of 100 - 500 ppm.

62.12%, 47.92% and 33.33% respectively. However, the best working temperature of the $SnO_2$ NB to the three gases are 220˚C and its responses are only 42.86%, 24.24% and 16.67%. Obviously, the sensitivity of Mn:$SnO_2$ NB is much better than that of the latter, especially to ethanol. The best working temperature of Mn:$SnO_2$ NB is lower and the sensitivity to ethanol reaches 62.12%, far higher to the others. As evidenced from Figure 7(c), the sensitive responses of Mn:$SnO_2$ NB for ethanol, ethanediol and acetone are 1.51, 1.45, and 1.25 times as

large as those of pure $SnO_2$ NB. The results manifest that doping of Mn reduces the optimum working temperature, enhances the sensitivity effectively, and greatly improves the selectivity of $SnO_2$ NB.

The response of the Mn:$SnO_2$ NB has also been tested and are illustrated in **Figure 7(d)**, **Figure 7(e)** under ethanol from 10 to 1000 ppm at 210˚C. It is noted that the response increased drastically in the range of 10 - 100 ppm, then moderately in 100 - 600 ppm, and slowly in 600 - 1000 ppm. The response tends to become saturated when ethanol concentration goes up, which can be attributed to the surface coverage of the adsorbed molecules [24]. The response of Mn:$SnO_2$ sensors are provided upon repeatedly ethanol, ethanediol, and acetone gases exposure/removal cycles, as displayed in **Figure 7(f)**. Five cycles are successively recorded, corresponding to 100, 200, 300, 400, and 500 ppm of ethanol gase. For all testing cycles, the resistance returns completely to its original value once the gases are pumped out. It can be seen that Mn:$SnO_2$ NB has a high sensitivity to ethanol. The corresponding response/recovery time is about 18 s/20 s.

**Figure 7(g)** shows the fitting curve of response versus ethanol concentration in the range of 100 - 500 ppm. The response is approximately linearly, and the slope of it is 0.0334 $ppm^{-1}$ with a fitting quality of $R = 0.9788$. The sensor noise is calculated by the variation of the relative response at the baseline with help of root-mean-square deviation (RMSD) [22] [23] [28]. Then, 200 data points ($N$) of **Figure 7(f)** are collected, and the standard deviation ($S$) is obtained as 0.17369. According to $RMS_{noise} = \sqrt{S^2/N}$, $RMS_{noise}$ is 0.01228 for the ethanol sensor. Based on the signal-to-noise ratio using $DL(ppm) = 3 \times RMS_{noise}/Slope$, the theoretical detection limit for ethanol of the sensor is 1.1 ppm.

### 3.4. Gas Sensing Mechanism

As a solid material, the gas-sensing mechanism of $SnO_2$ sensor belongs to surface phenomenon [29]. It is well known that the gas sensing involves three key reaction processes: adsorption, oxidation, and desorption [30]. The oxygens are adsorbed in several species such as $O_2^-$, $O^-$ and $O^{2-}$ through Equations (1)-(4) [31].

$$O_2\ (\text{Gas}) \Leftrightarrow O_2\ (\text{adsorption}) \tag{1}$$

$$O_2\ (\text{adsorption}) + e^- \Leftrightarrow O_2^-\ (\text{adsorption}) \tag{2}$$

$$O_2^-\ (\text{adsorption}) + e^- \Leftrightarrow 2O^-\ (\text{adsorption}) \tag{3}$$

$$O_2^-\ (\text{adsorption}) + e^- \Leftrightarrow O_2^-\ (\text{adsorption}) \tag{4}$$

when ethanol liquid is injected into the equipment and then evaporates, its vapor contacts the sensor and reacts with the surface chemisorbed oxygen. The process is as follows:

$$C_2H_5OH + 3O_2^-\ (\text{ads}) = 2CO_2 + 3H_2O + 3e^- \tag{5}$$

$$C_2H_5OH + 6O^-\ (\text{ads}) = 2CO_2 + 3H_2O + 6e^- \tag{6}$$

$$C_2H_5OH + 6O^{2-}\ (\text{ads}) = 2CO_2 + 3H_2O + 12e^- \tag{7}$$

Obviously, many electrons are released and hence the resistance decreases during the reaction. In our work, the sensitivity to ethanol is availably improved by Mn ions. The reasonable sensitive improvement mechanism is proposed as follows. As shown as the results, Mn ions can promote the crystallinity of $SnO_2$ NBs. Besides, Mn doping can produce more oxygen vacancies and reduces the barrier height of the material [32].

$$Mn^{3+} + H_2O \rightarrow MnO^{+} + H^{+} \quad (8)$$

$$O_O^{\times} \leftrightarrow V_O^{\bullet\bullet} + 2e' + 1/2O_2 \quad (9)$$

$$2MnO^{+} + O_O^{\times} \rightarrow Mn_2O_3 + V_O^{\bullet\bullet} + 2e' \quad (10)$$

As expressed by Equations (8)-(10), Mn ions may enhance the surface dehydrogenation resulting in the oxidation of ethanol needs lower energy, so that the liberation of electrons will be promoted [33] [34]. Hence, the electric conductivity of $SnO_2$ NB increases.

## 4. Conclusion

Mn:$SnO_2$ NBs and pure $SnO_2$ NBs were synthesized by thermal evaporation. The band gap of Mn doped $SnO_2$ nanobelts by UV-Vis was measured and is 3.43 eV respectively at room temperature, lower than that of the pure $SnO_2$ NBs (~3.66 eV). $SnO_2$ NB and Mn:$SnO_2$ NB sensors were developed. It is found that the Mn:$SnO_2$ NB device exhibits a higher sensitivity of 62.12% to 100 ppm of ethanol at 210˚C, which is the highest sensitivity among the three tested VOC gases. The higher response is related to the selective catalysis of doped Mn ions.

## Acknowledgments

This work was supported by the National Natural Science Foundation (Grant No. 11164034), the Key Applied Basic Research Program of Science and Technology Commission Foundation of Yunnan Province (Grant No. 2013FA035), and the Innovative talents of Science and Technology Plan Projects of Yunnan Province (Grant No. 2012HA007).

## References

[1] Ahn, J.H., Yun, J., Choi, Y.K. and Park, I. (2013) Palladium Nanoparticle Decorated Silicon Nanowire Field-Effect Transistor with Side-Gates For Hydrogen Gas Detection. *Applied Physics Letters*, **104**, Article ID: 013508.

[2] Liu, X., Zhang, J., Yang, T., Guo, X., Wu, S. and Wang, S. (2011) Synthesis of Pt Nanoparticles Functionalized $WO_3$ Nanorods and Their Gas Sensing Properties. *Sensors and Actuators B*: *Chemical*, **156**, 918-923. https://doi.org/10.1016/j.snb.2011.03.006

[3] Herrera, M., Maestre, D., Cremades, A. and Piqueras, J. (2013) Growth and Characterization of Mn Doped $SnO_2$ Nanowires, Nanobelts, and Microplates. *The Journal of Physical Chemistry C*, **117**, 8997-9003. https://doi.org/10.1021/jp4007894

[4] Choi, S.W., Katoch, A., Sun, G.J., Wu, P. and Kim, S.S. (2013) $NO_2$-Sensing Performance of $SnO_2$ Microrods by Functionalization of Ag Nanoparticles. *Journal of Materials Chemistry C*, **1**, 2834-2841. https://doi.org/10.1039/c3tc00602f

[5] Tonezzera, M. and Hieu, N.V. (2012) Size-Dependent Response of Single-Nanowire

Gas Sensors. *Sensors and Actuators B*: *Chemical*, **163**, 146-152. https://doi.org/10.1016/j.snb.2012.01.022

[6] Shao, F., Hoffmann, M.W.G., Prades, J.D., Zamani, R., Arbiol, J. and Morante, J.R. (2013) Heterostructured p-CuO (Nanoparticle)/n-$SnO_2$ (Nanowire) Devices for Selective $H_2S$ Detection. *Sensors and Actuators B*: *Chemical*, **181**, 130-135.

[7] Fang, X.S., Wu, L.M. and Hu, L.F. (2011) ZnS Nanostructure Arrays: A Developing Material Star. *Advanced Materials*, **23**, 585-598. https://doi.org/10.1002/adma.201003624

[8] Wang, L., Chen, Y., Ma, J., Chen, L., Xu, Z. and Wang, T. (2013) Hierarchical $SnO_2$ Nanospheres: Bio-Inspired Mineralization, Vulcanization, Oxidation Techniques, and the Application for NO Sensors. *Scientific Reports*, **3**, 3500.

[9] Wang, Y., Liu, B., Cai, D., Li, H., Liu, Y., Wang, D., Wang, L., Li, Q. and Wang, T. (2014) Room-Temperature Hydrogen Sensor Based on Grain-Boundary Controlled Pt Decorated $In_2O_3$ Nanocubes. *Sensors and Actuators B*: *Chemical,* **201**, 351-359 .

[10] Quang, V.V., Dung, N.V., Trong, N.S., Hoa, N.D., Duy, N.V. and Hieu, N.V. (2014) Outstanding Gas-Sensing Performance of Graphene/$SnO_2$ Nanowire Schottky Junctions. *Applied Physics Letters*, **105**, Article ID: 013107.

[11] Liu, X., Zhang, J., Guo, X., Wu, S. and Wang, S. (2010) Amino Acid-Assisted One-Pot Assembly of Au, Pt Nanoparticles Onto One-Dimensional ZnO Microrods. *Nanoscale*, **2**, 1178-1184. https://doi.org/10.1039/c0nr00015a

[12] Wang, H. and Rogach, A.L. (2014) Hierarchical $SnO_2$ Nanostructures: Recent Advances in Design, Synthesis, and Applications. *Chemistry of Materials*, **26**, 123-133. https://doi.org/10.1021/cm4018248

[13] Tricoli, A. and Pratsinis, S.E. (2010) Dispersed Nanoelectrode Devices. *Nature Nanotechnology*, **5**, 54-60. https://doi.org/10.1038/nnano.2009.349

[14] Cai, B., Zhao, X., Pei, T., Toninelli, E., Tang, Q., Tong, Y. and Liu, Y. (2014) Conductive $SnO_2$: Sb Nanobelts as Electrodes for Detection of $NO_2$ in Ppb Level with Ultrahigh Sensitivity. *Applied Physics Letters*, **104**, Article ID: 073112.

[15] Lu, G., Ocola, L.E. and Chen, J. (2009) Room-Temperature Gas Sensing Based on Electron Transfer between Discrete tin Oxide Nanocrystals and Multiwalled Carbon Nanotubes. *Advanced Materials*, **21**, 2487-2491. https://doi.org/10.1002/adma.200803536

[16] Li, X., Zhang, F. and Zhao, D. (2015) Lab on up Conversion Nanoparticles: Optical Properties and Applications Engineering via Designed Nanostructure. *Chemical Society Reviews*, **44**, 1346-1378. https://doi.org/10.1039/C4CS00163J

[17] Wang, H., Lu, W., Zeng, T., Yi, Z., Rao, L., Liu, H. and Zeng, S. (2014) Multi-Functional $NaErF_4$: Yb Nanorods: Enhanced Red Upconversion Emission, *in Vitro* Cell, *in Vivo* X-Ray, and $T_2$-Weighted Magnetic Resonance Imaging. *Nanoscale*, **6**, 2855-2860. https://doi.org/10.1039/c3nr05782h

[18] Epicier, T., Boulon, G., Zhao, W., Guzik, M., Jiang, B., Ikesuef, A. and Esposito, L. (2012) Spatial Distribution of the $Yb^{3+}$ Rare Earth Ions in $Y_3Al_5O_{12}$ and $Y_2O_3$ Optical Ceramics as Analyzed by TEM. *Journal of Materials Chemistry*, **22**, 18221-18229. https://doi.org/10.1039/c2jm32995f

[19] Zhang, K.C., Li, Y.F., Liu, Y. and Chi, F. (2014) Density-Functional Study on the Robust Ferromagnetism in Rare-Earth Element Yb-Doped $SnO_2$. *Journal of Magnetism and Magnetic Materials*, **360**, 165-168. https://doi.org/10.1016/j.jmmm.2014.02.054

[20] Bouzidi, C., Elhouichet, H. and Moadhen, A. (2011) $Yb^{3+}$ Effect on the Spectroscopic Properties of Er-Yb Codoped $SnO_2$ Thin Films. *Journal of Luminescence*, **131**,

2630-2635. https://doi.org/10.1016/j.jlumin.2011.06.040

[21] Wang, T.T., Ma, S.Y., Cheng, L., Luo, J., Jiang, X.H. and Jin, W.X. (2015) Preparation of Yb-Doped $SnO_2$ Hollow Nanofibers with an Enhanced Ethanol-Gas Sensing Performance by Electrospinning. *Sensors and Actuators B*: *Chemical*, **216**, 212-220.

[22] Chen, W.W., Liu, Y.K., Qin, Z.J., Wu, Y.M., Li, S.H. and Ai, P. (2015) A Single Eu-Doped $In_2O_3$ Nanobelt Device for Selective $H_2S$ Detection. *Sensors*, **15**, 29950-29957. https://doi.org/10.3390/s151229775

[23] Qin, Z.J., Liu, Y.K., Chen, W.W., Ai, P., Wu, Y.M., Li, S.H. and Yu, D.P. (2016) Highly Sensitive Alcohol Sensor Based on a Single Er-Doped $In_2O_3$ Nanoribbon. *Chemical Physics Letters*, **646**, 12-17. https://doi.org/10.1016/j.cplett.2015.12.054

[24] Michel, C.R., Martínez-Preciadob, A.H. and Rivera-Tello, C.D. (2015) $CO_2$ Gas Sensing Response of $YPO_4$ Nanobelts Produced by a Colloidal Method. *Sensors and Actuators B*: *Chemical*, **221**, 499-506.

[25] Zhao, Z., Tian, J., Sang, Y., Cabot, A. and Liu, H. (2015) Structure, Synthesis, and Applications of $TiO_2$ Nanobelts. *Advanced Materials*, **27**, 2557-2582. https://doi.org/10.1002/adma.201405589

[26] Cheng, L., Ma, S.Y., Li, X.B., Luo, J., Li, W.Q., Li, F.M., Mao, Y.Z., Wang, T.T. and Li, Y.F. (2014) Highly Sensitive Acetone Sensors Based on Y-Doped $SnO_2$ Prismatic Hollow Nanofibers Synthesized by Electrospinning. *Sensors and Actuators B*: *Chemical*, **200**, 181-190.

[27] Samà, J., Barth, S., Domènech-Gil, G., Prades, J.D., Romano-Rodríguez, A., López N. and Casals, O. (2016) Site-Selectively Grown $SnO_2$ NWs Networks on Micromembranes for Efficient Ammonia Sensing in Humid Conditions. *Sensors and Actuators B*: *Chemical*, **232**, 402-409.

[28] Yang, W., Wan, P., Zhou, X.D., Hu, J.M., Guan, Y.F. and Feng, L. (2014) An Additive-Free Synthesis of $In_2O_3$ Cubes Embedded into Grapheme Sheets and Their Enhanced $NO_2$ Sensing Performance at Room Temperature. *ACS Applied Materials & Interfaces*, **6**, 21093-21100. https://doi.org/10.1021/am505949a

[29] Chen, P.C., Sukcharoenchoke, S., Ryu, K., Arco, L.G.D., Badmaev, A., Wang, C. and Zhou, C. (2010) 2, 4, 6-Trinitrotoluene (TNT) Chemical Sensing Based on Aligned Single-Walled Carbon Nanotubes and ZnO Nanowires. *Advanced Materials*, **22**, 1900-1904.

[30] Dua, V., Surwade, S.P., Ammu, S., Agnihotra, S.R., Jain, S., Roberts, K.E., Park, S. and Ruoff, R.S. (2010) Manohar, All-Organic Vapor Sensor Using Inkjet-Printed Reduced Graphene Oxide. *Angewandte Chemie*, **122**, 2200-2203. https://doi.org/10.1002/ange.200905089

[31] Yuan, W., Liu, A., Huang, L., Li, C. and Shi, G. (2013) High-Performance $NO_2$ Sensors Based on Chemically Modified Graphene. *Advanced Materials*, **25**, 766-771. https://doi.org/10.1002/adma.201203172

[32] Wagner, T., Haffer, S., Weinberger, C., Klaus, D. and Tiemann, M. (2013) Mesoporous Materials as Gas Sensors. *Chemical Society Reviews*, **42**, 4036-4053. https://doi.org/10.1039/C2CS35379B

[33] Xu, K., Zeng, D., Tian, S., Zhang, S. and Xie, C. (2014) Hierarchical Porous $SnO_2$ Micro-Rods Topologically Transferred from Tin Oxalate for Fast Response Sensors to Trace Formaldehyde. *Sensors and Actuators B*: *Chemical*, **190**, 585-592.

[34] Li, Y.S., Xu, J., Chao, J.F., Chen, D., Ouyang, S.X., Ye, J.H. and Shen, G.Z. (2011) High-Aspect-Ratio Single-Crystalline Porous $In_2O_3$ Nanobelts with Enhanced Gas Sensing Properties. *Journal of Materials Chemistry*, **21**, 12852-12857. https://doi.org/10.1039/c1jm11356a